Inorganic Chemistry
Cite This: Inorg. Chem. 2019, 58, 13953−13959
Article
pubs.acs.org/IC

Room Temperature Lead-Free Multiaxial Inorganic−Organic Hybrid Ferroelectric

Bin Wang,[#] Dangwu Ma,[#] Haixia Zhao,*[] Lasheng Long,*[] and Lansun Zheng

Collaborative Innovation Center of Chemistry for Energy Materials, State Key Laboratory of Physical Chemistry of Solid Surfaces and Department of Chemistry, College of Chemistry and Chemical Engineering, Xiamen University, Xiamen 361005, PR China

Supporting Information

ABSTRACT: In recent years, molecular ferroelectrics have received more and more attention. Nevertheless, the study of multiaxial molecular ferroelectrics is relatively rare, which significantly restricts the development of their applications in thin films and other potential fields. Here we demonstrate the characteristics of a room-temperature lead-free multiaxial inorganic−organic hybrid ferroelectric material $[(CH_3)_2NH_2][C_6H_5CH_2NH_3]_2BiBr_6$ (**1**), which goes through a distinctly reversible phase transition around 386 K and possesses six equivalent ferroelectric directions. At 330 K, the remnant polarization (P_r) of **1** is ∼1.0 $\mu C \cdot cm^{-2}$, and the coercive field (E_c) of **1** is 20 $kV \cdot cm^{-1}$. The multiaxial and switching polarization behaviors of **1** were declared with piezoresponse force microscopy (PFM). Notably, the emergence of six equivalent ferroelectric directions is induced by the easily disordered cations and highly geometrically symmetrical anions, because they usually lead to a large symmetry change in the order−disorder types of ferroelectrics. This work provides an effective approach to construct molecular multiaxial ferroelectrics.

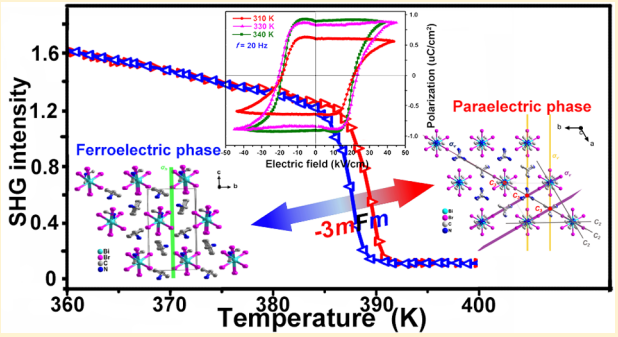

INTRODUCTION

As one of the most researched and exploited types of polar materials, ferroelectrics have been widely used in ferroelectric random access memory (FeRAM), capacitors, and nonlinear optical components.[1−5] Spontaneous polarization can be reoriented under an applied electric field for the ferroelectric materials, which is a distinguishing characteristic compared to other polar pyroelectric materials. Molecular ferroelectrics are particularly interesting because of their low toxicity, easy preparation, and flexible machinability when compared with the inorganic ceramic ferroelectrics.[6,7]

A ferroelectric single crystal should be measured along the spontaneous polarization vector, which is a specific direction (the ferroelectric polarization direction), to obtain the maximal polarization. For a uniaxial ferroelectric, polarization switching could only be achieved along the single ferroelectric polarization axis, and a deviation of direction would cause either the reduction or disappearance of polarization. Meanwhile, polarization switching can be along multiple directions in a multiaxial ferroelectric. Multiaxial ferroelectrics are more desirable for use in practical applications of molecular ferroelectrics, because the switchable polarization can be realized in polycrystalline states, such as thin films, powder pellets, and so on.[8,9] For example, the molecular ferroelectric $[N(CH_3)_4][GaCl_4]$ possesses 12 equivalent polarization directions, and the remnant polarization value could be 3.8 $\mu C \cdot cm^{-2}$ in free-standing film samples; this value is just slightly below the theoretical value (4.37 $\mu C \cdot cm^{-2}$).[10]

The quantity of equivalent ferroelectric directions is a key factor for multiaxial ferroelectric materials.[11] According to the Aizu rule,[12] the structural symmetry change between the paraelectric and ferroelectric phase determines the quantity of equivalent polarization directions. The specific number of polarization directions can be calculated according to the equation: $n = N_p/N_f$, where n represents the number of orientation states (equivalent polarization directions) and N_p and N_f represent the number of symmetric elements in the point group of the paraelectric phase and ferroelectric phase, respectively.[13,14] Current reported molecular ferroelectrics are mostly order−disorder types of molecular−ionic compounds, in which ferroelectric transition is induced by the order−disorder dynamic ions.[15−17] From this, the easily disordered cations and highly geometrically symmetrical anions are chosen to explore new multiaxial ferroelectrics, as these ions usually show high symmetry at the high temperature and translate into an ordered low-symmetry phase at the low temperature. To date, although the design of ferroelectric materials has improved, multiaxial molecular ferroelectrics are still rare and need further investigation.

Most of the single-cation Bi-based compounds crystallize in a centrosymmetric space group.[18,19] Coexistence of two types of organic cations may not only reduce the structural symmetry, but also improve the probability of multipolar axis.[20−22] In this

Received: June 25, 2019
Published: September 26, 2019

DOI: 10.1021/acs.inorgchem.9b01793
Inorg. Chem. 2019, 58, 13953−13959

work, two types of easily disordered cations (dimethylammonium and benzylammonium cations) with different configurations, which were often used alone to construct ferroelectrics, were chosen to induce the multiaxial ferroelectricity. Successfully, we synthesized a room-temperature lead-free multiaxial inorganic−organic hybrid ferroelectric material, $[(CH_3)_2NH_2][C_6H_5CH_2NH_3]_2BiBr_6$ (**1**). Compound **1** exhibits a distinct point group transition from paraelectric $\bar{3}m$ to ferroelectric m at approximately 386 K. The calculated n is six, indicating that **1** is a multiaxial ferroelectric and possesses six equivalent polarization directions. The ferroelectric behavior was measured and the remnant polarization (P_r) was around 1.0 $\mu C \cdot cm^{-2}$ with a large coercive field (E_c) of 20 $kV \cdot cm^{-1}$ at 330 K. Additionally, piezoresponse force microscopy (PFM) measurements were performed to confirm the switching behaviors and multiaxial ferroelectricity of **1**. This work provides an effective approach to construct multiaxial molecular ferroelectrics.

EXPERIMENTAL DETAILS

Preparation. All reagents and solvents were purchased from Heowns Biochem Technologies, LLC, and used without any further purification in the synthesis. An excess of concentrated hydrobromic acid (2 mL, 40 wt %) was added to bismuth(III) bromide (1 mmol, ≥ 97%) in methanol (20 mL). The solution was then added to dimethylamine (1 mmol) and phenethylamine (2 mmol) while heating at 80 °C. Pale yellow crystals of **1** can be obtained by cooling and evaporating the solution at room temperature for several days (total yield: 85%, based on $BiBr_3$). The platelike crystals of **1** were washed with methanol and dried under vacuum for 24 h.

Powder X-ray diffraction (PXRD) and elemental analysis confirmed the purity of the samples of **1** (Figure S1). The results from elemental analysis of **1** were as follows: Calculated (%): C 18.18, H 4.54, and N 1.30. Found (%): C 18.16, H 4.51, and N 1.27.

Single-Crystal Structures Determination. Variable-temperature single X-ray diffractions were employed by an Agilent Supernova CCD diffractometer with ω-scan mode ($\Delta\omega$ = 1.0°). The low temperature phase (LTP, 100 K, 300 K) and high temperature phase (HTP, 400 K) were performed with Mo Kα (λ = 0.71073 Å) and Cu Kα (λ = 1.54178 Å) radiation, respectively. Data collection, cell refinement, and data reduction were carried out in the CrysAlis PRO program. The crystal structures were solved by direct methods (*ShelXT*),[23] and refined by the full-matrix least-squares method based on F^2 with all non-hydrogen atoms anisotropic by using the *ShelXL* in the *OLEX2* program.[24,25] The positions of all hydrogen atoms were refined using a riding model. The hydrogen atoms in the HTP were not added because of the highly disordered dimethylammonium and benzylammonium cations. Because the distance between the acceptors (Br) and donors (N) is longer than 3.2 Å, the hydrogen-bonding interactions are disregarded in both the HTP and LTP (Figure S2). CCDC 1921186 (**1**-LTP, 100 K), CCDC 1945996 (**1**-LTP, 300 K), and 1921179 (**1**-HTP, 400 K), which can be obtained free of charge from the Cambridge Crystallographic Data Centre, contain the supplementary crystallographic data for this paper. Crystallographic data of **1** at different temperatures are shown in Table 1.

Physical Measurements. PXRD measurements were collected using a Rigaku Ultima IV X-ray diffractometer and a Bruker D8 Discover X-ray Powder Diffractometer for room- and variable-temperature PXRD patterns, respectively. Variable-temperature PXRD patterns were performed in air atmospheres at 300, 350, and 400 K. The powder sample of **1** was placed for 10 min at each test temperature before PXRD measurements.

Thermogravimetric analysis (TGA) measurement were employed by an SDT-Q600 thermal analyzer (TA Instruments) under an air atmosphere in alumina crucibles with a heating rate of 10 $K \cdot min^{-1}$(Figure S3). Differential scanning calorimetry (DSC) measurements were collected using a NETZSCH DSC 200F3 instrument with heating and cooling rates of 10 $K \cdot min^{-1}$ (the mass of the sample is 6.804 mg) under nitrogen atmospheres.

Table 1. Crystal Data of 1 at Different Temperatures[a]

compound	$[(CH_3)_2NH_2][C_6H_5CH_2NH_2]_2BiBr_6$ (**1**)	
temperature (K)	100.00(10)	400.00(10)
phase	LTP	HTP
formula weight	950.85	950.85
crystal system	monoclinic	trigonal
space group	*Pc*	$P\bar{3}m1$
a (Å)	10.25447(14)	8.6969(4)
b (Å)	8.45982(13)	8.6969(4)
c (Å)	14.4510(2)	10.2622(7)
α (deg)	90	90
β (deg)	90.8677(13)	90
γ (deg)	90	120
volume (Å^3)	1253.50(3)	672.20(8)
Z	2	1
scan mode	ω-scan	ω-scan
μ (mm^{-1})	16.603	23.365
$F(000)$	876.0	410.0
crystal size (mm^3)	0.2 × 0.2 × 0.1	0.3 × 0.2 × 0.1
radiation	Mo Kα	Cu Kα
wavelength (Å)	0.71073	1.54178
2θ range for data collection (deg)	6.826−51.988	8.616−125.758
index ranges	$-12 \le h \le 12$	$-6 \le h \le 7$
	$-10 \le k \le 10$	$-9 \le k \le 9$
	$-17 \le l \le 17$	$-11 \le l \le 10$
density ($g\ cm^{-3}$)	2.519	2.279
reflections collected	17349	1166
R_{int}	0.0465	0.0286
refinement method	full-matrix least-squares on F^2	
data/restraints/parameters	4925/14/215	446/66/44
goodness-of-fit on F^2	1.110	1.152
R_1, ωR_2 [$I > 2\sigma(I)$]	0.0489, 0.1073	0.0715, 0.1692
R_1, ωR_2 [all data]	0.0499, 0.1079	0.0719, 0.1695
ρ_{max}, ρ_{min} (e Å^{-3})	1.98, −1.56	1.59, −2.35

[a] $R_1 = \sum||F_o| - |F_c||/\sum|F_o|$, $\omega R_2 = \{\sum[\omega(|F_o|^2 - |F_c|^2)]/\sum[\omega|F_o|^4]\}^{1/2}$ and $\omega = 1/[\sigma^2(F_o^2) + (0.1361P)^2]$ for HTP and $\omega = 1/[\sigma^2(F_o^2) + (0.0001P)^2 + 56.7882P]$ for LTP, where $P = (F_o^2 + 2F_c^2)/3$.

The polarization−electric field (P−E) hysteresis loops were performed on a Radiant Precision Premier II analyzer using the positive up negative down (PUND) method, which can eliminate the small electrical conductivity contributions. The temperature of the sample was controlled by a Janis cryogenic refrigeration system under vacuum.

The dielectric permittivity, ε ($\varepsilon = \varepsilon' - i\varepsilon''$), measurements were employed by a Wayne Kerr 6500B analyzer using the two-probe ac impedance method over the frequency range from 100 Hz to 1 MHz. Powder pressed pellets with silver paste as the two electrodes were used for dielectric measurements.

The second harmonic generations (SHG) measurements were employed by an unexpanded laser beam (OPOTEK, 355 II) with low divergence (pulsed Nd:YAG, 1064 nm, 5 ns, 10 Hz repetition rate, 1.6 MW peak power). The numeral values of nonlinear optical numerical coefficients of **1** for the SHG were determined by comparison with those of potassium dihydrogen phosphate (KDP, $\chi_{KDP}^{(2)}$ = 0.39 $pm \cdot V^{-1}$).

The piezoresponse force microscopy (PFM) measurements were collected using a commercial piezoresponse force microscope (Cypher, Asylum Research) by using conductive Pt-/Ir-coated silicon probes (EFM-20, Nanoworld). PFM measurements were all performed on crystal samples.

DOI: 10.1021/acs.inorgchem.9b01793
Inorg. Chem. 2019, 58, 13953−13959

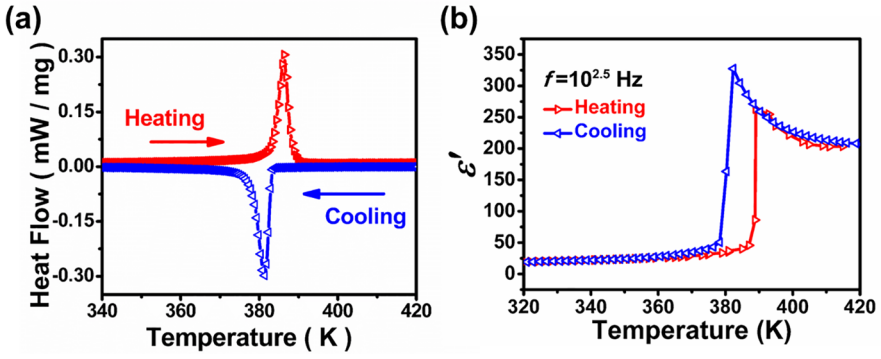

Figure 1. (a) DSC curves of **1**. (b) Temperature dependence of dielectric real parts (ε') for **1** at $10^{2.5}$ Hz measured on a powder sample.

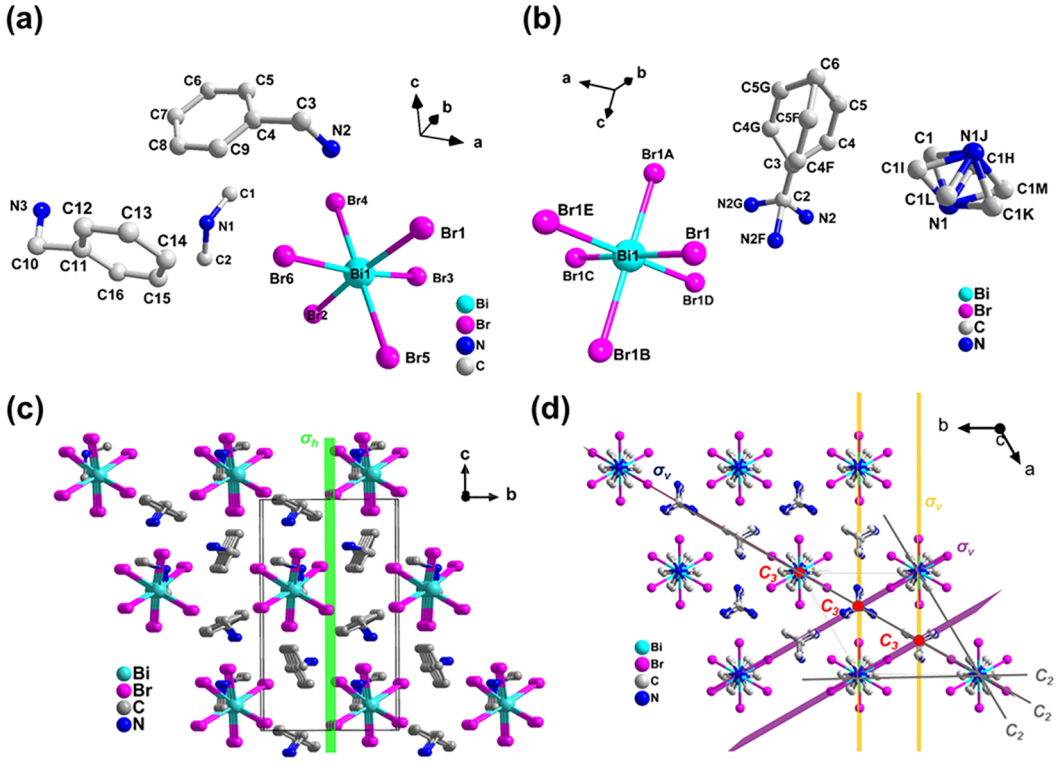

Figure 2. Asymmetric unit of **1** in (a) the LTP and (b) the HTP. Perspective views of **1** in the LTP along the *a*-axis (c) and the same view (d) in the HTP. All hydrogen atoms were omitted for clarity. Symmetry codes: A. $2+y-x, 1-x, z$; B. $-y+x, -1+x, 1-z$; C. $2-x, -y, 1-z$; D. $1+y, 1-x+y, 1-z$; E. $1-y, -1+x-y, z$; F. $1-y, x-y, z$; G. $1+y-x, 1-x, z$; H. $-y+x, x, -z$; I. $y, -x+y, -z$; J. $y, x, -z$; K. $-x, -y, -z$; L. $y-x, -x, z$; M. $-y, x-y, z$.

RESULTS AND DISCUSSION

DSC unambiguously revealed that **1** goes through a phase transition at ca. 386 K on heating, and the corresponding phase transition on cooling is observed ca. 381 K (Figures 1a and S4). The entropy change (ΔS) to concomitant the transitions is calculated with a value of 14.68 $J \cdot mol^{-1} \cdot K^{-1}$. According to the Boltzmann equation, $\Delta S = R \ln N$, where R denotes the gas constant and N represents the ratio of numbers of possible orientations for the disordered system. The N values for the transitions is 5.82, which indicates a typical order−disorder phase transition. To further disclose the phase transition, the dielectric constant varying with different temperatures was measured from 320 to 420 K (Figure 1b). The dielectric real parts (ε') keep almost constant (ca. 25) from 320 to 360 K. Upon increasing the temperature, the ε' increases sharply from ca. 47 to 265 at approximately 390 K and exhibits a steplike rising dielectric anomaly, indicating that a phase transition has occurred at ca. 390 K. This dielectric anomaly corresponds to the phase transition on the DSC curves. With further temperature increase, ε' decreases very slowly and then remains almost constant (ca. 202). Comparing the heating and cooling processes, a large thermal hysteresis of ca. 9 K can be found in the phase transition, which is consistent with the DSC result. Meanwhile, the dielectric constants exhibit no obvious frequency dependence below 386 K. In contrast, the dielectric constants decrease with increasing frequency once above 386 K (Figure S5).

To reveal the mechanism of the phase transition, the variable-temperature single-crystal data of **1** were collected at 100, 300, and 400 K. At 100 K (LTP), **1** crystallizes in the monoclinic system with a polar space group of *Pc*. The asymmetric unit of **1** consists of one isolated $[BiBr_6]^{3-}$ anion, two protonated

DOI: 10.1021/acs.inorgchem.9b01793
Inorg. Chem. 2019, 58, 13953−13959

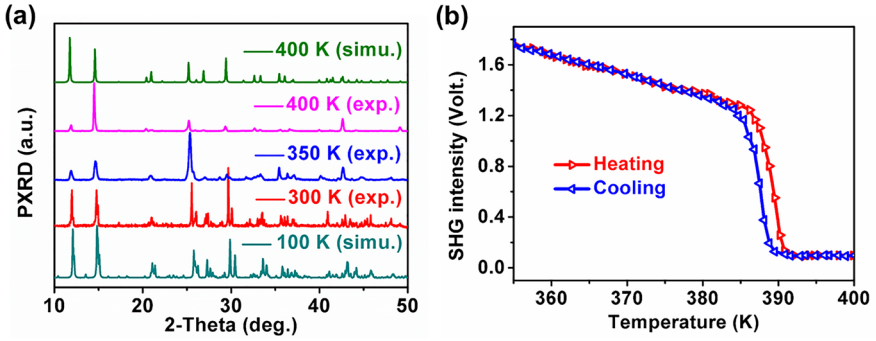

Figure 3. Variable-temperature PXRD patterns (a) and variable-temperature SHG signals (b) of **1**.

benzylammonium cations, and one protonated dimethylammonium cation in the LTP (Figure 2a). Obviously, both the dimethylammonium and benzylammonium cations are ordered, and the $BiBr_6$ octahedron architecture is slightly distorted because of the presence of a lone pair of *s* electrons (Figure S6a).[26,27] There is no phase transition from 100 to 386 K (Figure S7). At 300 K, **1** has the same structure as that at 100 K (Table S1). At 400 K (in the HTP), **1** crystallizes in the trigonal system with a centrosymmetric space group of $P\bar{3}m1$. The asymmetric unit of **1** is composed of one-sixth of an isolated $[BiBr_6]^{3-}$ anion, one-third of a protonated benzylammonium cation, and one-sixth of a protonated dimethylammonium cation, as shown in Figure 2b. Both the dimethylammonium and benzylammonium moieties are obviously disordered in the HTP. The benzylammonium cations are 3-fold disordered. Meanwhile, the two C atoms split into three positions, and the N atoms are 2-fold disordered along the *c* axis in the dimethylammonium cations. The $BiBr_6$ octahedrons adopt a high-symmetry configuration in the HTP (Figure S6b). As depicted in Figure 2c,d, in the crystal lattice, the isolated $[BiBr_6]^{3-}$ anions are sandwiched between two dimethylammonium cations along the *c* axis. The benzylammonium cations are inserted into adjacent dimethylammonium cations and isolated $[BiBr_6]^{3-}$ anions. The adjacent benzylammonium cations are antiparallel, but they display different orientations in the LTP. The arrangement of **1** is similar to the previously reported $(C_6H_5CH_2NH_3)_2[SnCl_6]$.[28]

From the point of view of symmetry, the polar space group of *Pc* has a lower noncentrosymmetric point group *m*, which possesses only two symmetric elements (*e* and σ_h) with the ordered cations and distorted $[BiBr_6]^{3-}$ anions in the LTP of **1** (Figure 2c). In the HTP, the centrosymmetric space group of $P\bar{3}m1$, which has a higher centrosymmetric point group $\bar{3}m$ with 12 symmetric elements (*e*, 2 C_3, 3 C_2, *i*, 2 S_6, and 3 σ_v). For organic cations, the benzylammonium and dimethylammonium cations turn into highly disordered in the HTP. The N atoms in the dimethylammonium cations, three carbon atoms of benzylammonium cations (C2, C3, and C6 in Figure 2b) and the Bi atoms in $BiBr_6$ octahedron are located in the 3-fold rotation axis, while all the other atoms of **1** satisfy the crystallographic symmetry of 3-fold rotation axis in the HTP (Figure 2d). Therefore, the phase transition of **1** contributed to the order−disorder of cations and the configuration change of anions.

Variable-temperature PXRD measurements were performed to indicate the structural phase transition. Based on the single-crystal structures of the LTP and HTP, the experimental PXRD patterns at 300 and 400 K, respectively, is in accordance with the corresponding simulated results (Figure 3a). Furthermore, temperature-dependent SHG measurements were measured to confirm breakage of the structural symmetry. As shown in Figure 3b, **1** has no SHG activity, and the SHG signal keeps at almost zero in HTP regions. In the LTP regions, **1** clearly exhibits SHG activity, which is ca. 0.77 times that of KDP (Figure S8). These results demonstrate compound **1** crystallizes in a polar space group in the LTP. Above all, the symmetry-breaking transition is regarded in the Aizu notation as $\bar{3}mFm$, which belongs to the 88 ferroelectric species. According to Aizu notation of $\bar{3}mFm$, the symmetric elements change from 12 symmetric elements (*e*, 2 C_3, 3 C_2, *i*, 2 S_6, and 3 σ_v) in the HTP to two (*e* and σ_h) in the LTP, and six polarization directions would be expected in the LTP.[12,29] This implies that **1** is a multiaxial ferroelectric.

Ferroelectric behavior is oriented in the polar direction and consists of the equivalent polarization directions. The crystal habit of **1** is plate-shaped. The direction perpendicular to the plate surface was determined to be the *b* direction by the data analysis software in the Agilent Supernova CCD diffractometer (Figure S9). According to the space groups of the LTP and HTP, the polar direction of **1** is in a certain direction on the *ac* plane in the LTP (Figure S10), and **1** possesses six equivalent polarization directions (Figure S11). As illustrated in Figure 4,

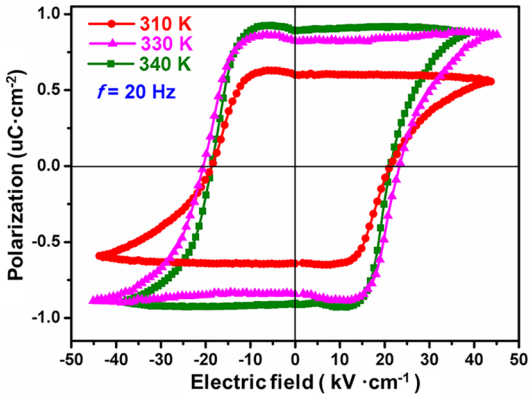

Figure 4. *P*−*E* hysteresis loops of **1** measured at different temperatures at a frequency of 20 Hz.

the variable-temperature *P*−*E* hysteresis loops of **1** were measured (the electric field was approximately parallel to the *c* direction). At 310 K, the P_r value is around 0.65 $\mu C \cdot cm^{-2}$. With the temperature increasing from 310 to 340 K, the P_r value increases slightly from 0.65 to 1.0 $\mu C \cdot cm^{-2}$, because the polarization reversal at lower temperature always needs a higher voltage. The coercive field is ca. 20 $kV \cdot cm^{-1}$, which is smaller

DOI: 10.1021/acs.inorgchem.9b01793
Inorg. Chem. 2019, 58, 13953−13959

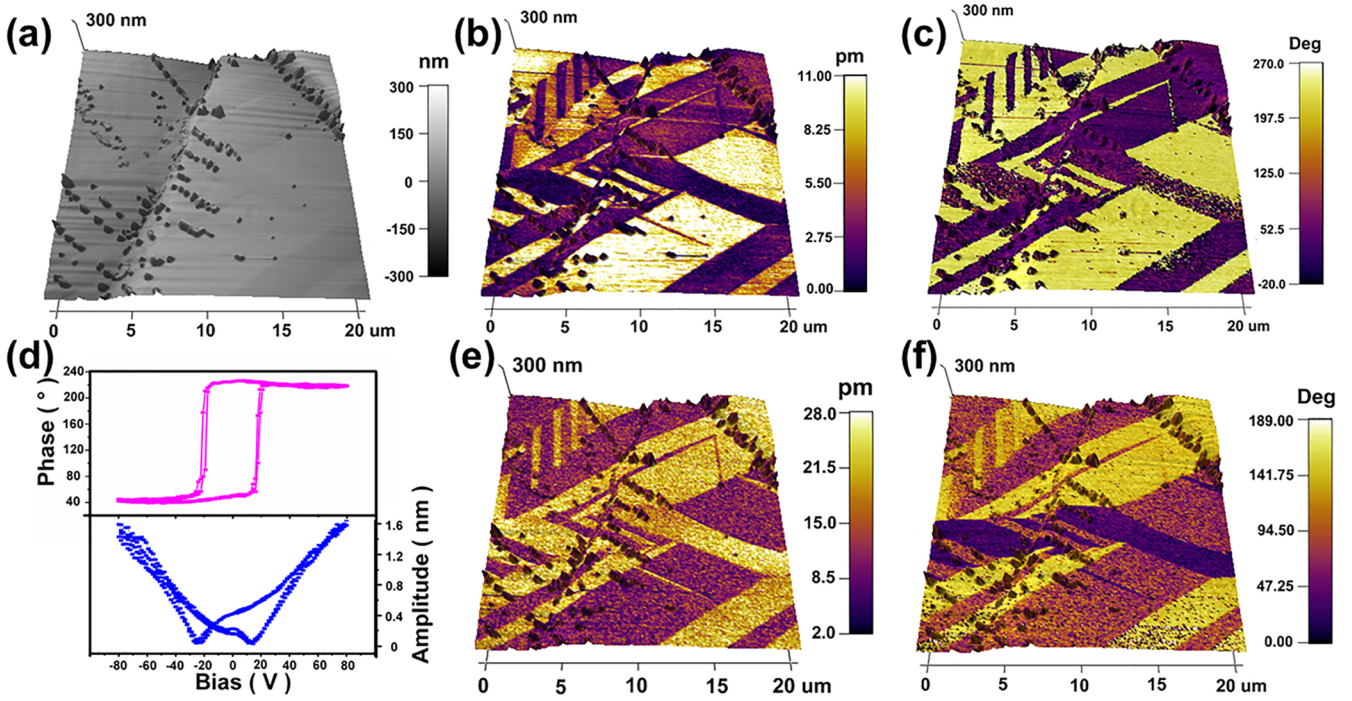

Figure 5. Vertical and lateral PFM images. (a) 3D topographic image of the crystal surface of **1**. Vertical and lateral PFM amplitude (b, e) and phase images (c, f) overlaid on 3D topography for the crystal of **1**. (d) Local PFM hysteresis loops for **1**.

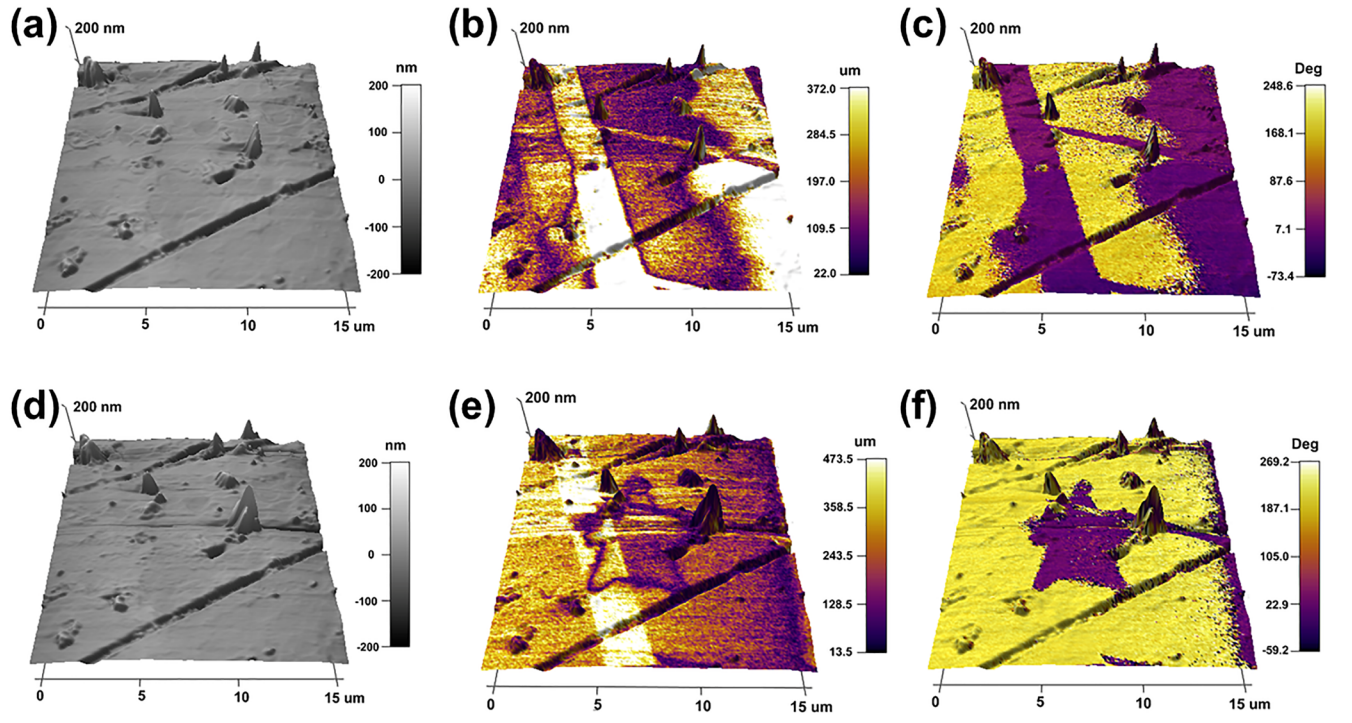

Figure 6. Topographic images (a), lateral PFM amplitude (b), and phase images (c) of the crystal surface overlaid on 3D topography in initial state. Topography image (d), lateral PFM amplitude (e), and phase images (f) of the crystal surface overlaid on 3D topography recorded after writing a star area with +80/−80 V.

than the ferroelectric poly(vinylidene) difluoride family (~500 $kV{\cdot}cm^{-1}$)[30] and [Hdabco]ClO_4 (~83 $kV{\cdot}cm^{-1}$).[31] Meanwhile, the P_r value of **1** is larger than most of the reported Bi-based molecular ferroelectrics, such as [imidazolium]$_5Bi_2Cl_{11}$ (~0.26 $\mu C{\cdot}cm^{-2}$),[32] and (pyridinium)$_5Bi_2Br_{11}$ (~0.3 $\mu C{\cdot}cm^{-2}$),[33] and is comparable with the recently reported [*N*,*N*-dimethyl-1,3-diaminopropane] [$SbCl_5$] (~1.36 $\mu C{\cdot}cm^{-2}$)[34] and $(C_2H_5NH_3)_2BiCl_5$ (~1.4 $\mu C{\cdot}cm^{-2}$).[35] However, the P_r value of compound **1** is still lower than that of other reported molecular ferroelectrics, for example, tetraethylammonium

DOI: 10.1021/acs.inorgchem.9b01793
Inorg. Chem. 2019, 58, 13953−13959

perchlorate (~7.0 μC·cm^{-2}),[11] and $[N(CH_3)_4]$ $[GaCl_4]$ (~3.8 μC·cm^{-2}),[10] indicating the need for further improvement.

PFM is a very useful visualization tool for the detection of ferroelectric domains with nondestructive the sample.[36,37] Amplitude and phase parameters with high spatial resolution can be obtained from PFM images, which can afford information about the orientation of polarization and the piezoelectric coefficient. To further expose the ferroelectric properties of **1**, PFM on the single-crystal surface was performed. As depicted in Figure 5, the vertical and lateral PFM amplitude and phase images were recorded in the same area of the crystal sample of **1** along the *ac* plane. These results directly prove the existence of ferroelectric domains, and this proof is a lack of significant correlation between phase images and topography image (Figure 5a,c,f).

Meanwhile, there is an obvious difference between the domain distributions in the vertical and lateral PFM modes. As depicted in Figure 5c,f, both phase images show antiparallel and non-180° domains in the vertical and lateral PFM modes, but these domains are located in different areas. Different ~180° and non-180° domains appear simultaneously in the out-of-plane and in-plane modes, indicating that there are different polarization directions in this region. This result corresponds well to the complex polarization directions. From these results, the ferroelectricity of **1** can be identified as having multiple polar axes.[38] The spontaneously polarized state of ferroelectrics will change under applied electricity or stress. Such domain switching is an important feature of ferroelectric materials. From the piezoresponse hysteresis loops measurements for the single-crystal samples of **1**, the phase hysteresis and amplitude butterfly loops exhibit 180° polarization switching of ferroelectric domains, which was triggered by the applied voltage (Figure 5d).

PFM lithography can "write" single domains, domain arrays, and complex patterns through the application of a bias voltage with nondestructive sample surface. To further characterize the switching behavior, a star pattern was written on the single-crystal sample surface of **1** in a selected 15 μm × 15 μm region by PFM lithography. In the initial state, the lateral PFM phase has an evident bipolar domain pattern, indicating that **1** is in a multidomain state at this selected in-plane region (Figure 6a–c). Meanwhile, the vertical PFM phase has a single domain pattern in this selected region (Figure S12). After the bias of +80/−80 V was applied in the probe tip, the color change in the lateral PFM phase images indicates that the polarization direction was switched in the star region. Specifically, uniform dark red and yellow colors can be observed in the internal and external regions of the star area (Figure 6d–f). The resultant star area with a large vertical phase contrast (~180°) and a single domain state proves that the polarization of **1** is undoubtedly switchable. The polarization switching back with opposite voltage revealed good ferroelectric retention of the crystal sample of **1**, which can rule out a possible origin of charging effects. The PFM results, along with the *P*–*E* loops, confirm that **1** can possess switchable polarization at room temperature, indicating directly that **1** is a ferroelectric material.

CONCLUSIONS

In summary, we have successfully explored a new room-temperature lead-free multiaxial inorganic–organic hybrid ferroelectric material, $[(CH_3)_2NH_2]$ $[C_6H_5CH_2NH_3]_2BiBr_6$ (**1**). Compound **1** has six polar directions, and the P_r equals to 1.0 μC·cm^{-2} at 330 K. The mechanisms of the ferroelectric in the LTP are related mostly to order–disorder of the organic cations, along with the distortion of $[BiBr_6]^{3-}$ anions. This work not only exhibits the multiaxial ferroelectricity in a lead-free inorganic–organic hybrid material but also provides an effective approach to construct molecular multiaxial ferroelectrics.

ASSOCIATED CONTENT

Supporting Information

The Supporting Information is available free of charge on the ACS Publications website at DOI: 10.1021/acs.inorgchem.9b01793.

PXRD patterns at room temperature; part of lengths (Å) of acceptors (Br) and donors (N) in HTP and LTP of **1**; TG curves of **1**; DSC curves of **1** at different scanning rates and at the temperature range of 100–425 K; dielectric constants measured with different frequencies; The comparison of $BiBr_6$ octahedron in LTP and HTP of **1**; SHG signals comparison diagram of **1** and KDP; Images of single crystal and directions of crystal; overall polarity of the structure line up in the crystallographic structure; Diagram of possible equivalent polarization directions of **1**; comparison diagram of after and before applied a +80/−80 V in vertical PFM; crystallographic data of **1** at 300 K (PDF)

Accession Codes

CCDC 1921179, 1921186, and 1945996 contain the supplementary crystallographic data for this paper. These data can be obtained free of charge via www.ccdc.cam.ac.uk/data_request/cif, or by emailing data_request@ccdc.cam.ac.uk, or by contacting The Cambridge Crystallographic Data Centre, 12 Union Road, Cambridge CB2 1EZ, UK; fax: +44 1223 336033.

AUTHOR INFORMATION

Corresponding Authors

*E-mail: hxzhao@xmu.edu.cn (H.-X.Z.).
*E-mail: lslong@xmu.edu.cn (L.-S.L.).

ORCID

Haixia Zhao: 0000-0002-1688-7713
Lasheng Long: 0000-0002-0398-4709

Author Contributions

#B.W. and D.-W.M. contributed equally to this work.

Notes

The authors declare no competing financial interest.

ACKNOWLEDGMENTS

This work was supported by the National Natural Science Foundation of China (Grant Nos. 21431005, 21721001, and 21571150) and the Fundamental Research Funds for the Central Universities of China (Grant No. 20720180030).

REFERENCES

(1) Scott, J. F. Applications of modern ferroelectrics. *Science* **2007**, *315*, 954–959.

(2) Xu, G.; Li, Y.; Zhou, W.-W.; Wang, G.-J.; Long, X.-F.; Cai, L.-Z.; Wang, M.-S.; Guo, G.-C.; Huang, J.-S.; Bator, G.; Jakubas, R. A ferroelectric inorganic-organic hybrid based on NLO-phore stilbazolium. *J. Mater. Chem.* **2009**, *19*, 2179–2183.

(3) Han, S.-T.; Zhou, Y.; Roy, V. A. L. Towards the Development of Flexible Non-Volatile Memories. *Adv. Mater.* **2013**, *25*, 5425–5449.

(4) Li, P.-F.; Tang, Y.-Y.; Liao, W.-Q.; Ye, H.-Y.; Zhang, Y.; Fu, D.-W.; You, Y.-M.; Xiong, R.-G. A semiconducting molecular ferroelectric with

DOI: 10.1021/acs.inorgchem.9b01793
Inorg. Chem. 2019, 58, 13953–13959

a bandgap much lower than that of $BiFeO_3$. *NPG Asia Mater.* **2017**, *9*, No. e342.
(5) Li, L.; Sun, Z.; Wang, P.; Hu, W.; Wang, S.; Ji, C.; Hong, M.; Luo, J. Tailored Engineering of an Unusual $(C_4H_9NH_3)_2(CH_3NH_3)_2Pb_3Br_{10}$ Two-Dimensional Multilayered Perovskite Ferroelectric for a High-Performance Photodetector. *Angew. Chem., Int. Ed.* **2017**, *56*, 12150−12154.
(6) Das, A.; Ghosh, S. Supramolekulare Anordnungen mit Charge-Transfer-Wechselwirkungen zwischen Donor- und Akzeptor-Chromophoren. *Angew. Chem.* **2014**, *126*, 2068−2084.
(7) Tayi, A. S.; Shveyd, A. K.; Sue, A. C. H.; Szarko, J. M.; Rolczynski, B. S.; Cao, D.; Kennedy, T. J.; Sarjeant, A. A.; Stern, C. L.; Paxton, W. F.; Wu, W.; Dey, S. K.; Fahrenbach, A. C.; Guest, J. R.; Mohseni, H.; Chen, L. X.; Wang, K. L.; Stoddart, J. F.; Stupp, S. I. Room-temperature ferroelectricity in supramolecular networks of charge-transfer complexes. *Nature* **2012**, *488*, 485−489.
(8) Harada, J.; Kawamura, Y.; Takahashi, Y.; Uemura, Y.; Hasegawa, T.; Taniguchi, H.; Maruyama, K. Plastic/Ferroelectric Crystals with Easily Switchable Polarization: Low-Voltage Operation, Unprecedentedly High Pyroelectric Performance, and Large Piezoelectric Effect in Polycrystalline Forms. *J. Am. Chem. Soc.* **2019**, *141*, 9349−9357.
(9) Harada, J.; Shimojo, T.; Oyamaguchi, H.; Hasegawa, H.; Takahashi, Y.; Satomi, K.; Suzuki, Y.; Kawamata, J.; Inabe, T. Directionally tunable and mechanically deformable ferroelectric crystals from rotating polar globular ionic molecules. *Nat. Chem.* **2016**, *8*, 946−952.
(10) Li, D.; Zhao, X.-M.; Zhao, H.-X.; Dong, X.-W.; Long, L.-S.; Zheng, L.-S. Construction of Magnetoelectric Composites with a Large Room-Temperature Magnetoelectric Response through Molecular-Ionic Ferroelectrics. *Adv. Mater.* **2018**, *30*, 1803716.
(11) Ye, H.-Y.; Ge, J.-Z.; Tang, Y.-Y.; Li, P.-F.; Zhang, Y.; You, Y.-M.; Xiong, R.-G. Molecular Ferroelectric with Most Equivalent Polarization Directions Induced by the Plastic Phase Transition. *J. Am. Chem. Soc.* **2016**, *138*, 13175−13178.
(12) Aizu, K. Possible Species of Ferromagnetic, Ferroelectric, and Ferroelastic Crystals. *Phys. Rev. B* **1970**, *2*, 754−772.
(13) Harada, J.; Yoneyama, N.; Yokokura, S.; Takahashi, Y.; Miura, A.; Kitamura, N.; Inabe, T. Ferroelectricity and Piezoelectricity in Free-Standing Polycrystalline Films of Plastic Crystals. *J. Am. Chem. Soc.* **2018**, *140*, 346−354.
(14) Tang, Y.-Y.; Li, P.-F.; Liao, W.-Q.; Shi, P.-P.; You, Y.-M.; Xiong, R.-G. Multiaxial Molecular Ferroelectric Thin Films Bring Light to Practical Applications. *J. Am. Chem. Soc.* **2018**, *140*, 8051−8059.
(15) Tang, Y. Z.; Yu, Y. M.; Xiong, J. B.; Tan, Y. H.; Wen, H. R. Unusual High-Temperature Reversible Phase-Transition Behavior, Structures, and Dielectric-Ferroelectric Properties of Two New Crown Ether Clathrates. *J. Am. Chem. Soc.* **2015**, *137*, 13345−13351.
(16) Huang, B.; Sun, L.-Y.; Wang, S.-S.; Zhang, J.-Y.; Ji, C.-M.; Luo, J.-H.; Zhang, W.-X.; Chen, X.-M. A near-room-temperature organic-inorganic hybrid ferroelectric: $[C_6H_5CH_2CH_2NH_3]_2[CdI_4]$. *Chem. Commun.* **2017**, *53*, 5764−5766.
(17) Szklarz, P.; Gągor, A.; Jakubas, R.; Zieliński, P.; Piecha-Bisiorek, A.; Cichos, J.; Karbowiak, M.; Bator, G.; Ciżman, A. Lead-free hybrid ferroelectric material based on formamidine: $[NH_2CHNH_2]_3Bi_2I_9$. *J. Mater. Chem. C* **2019**, *7*, 3003−3014.
(18) Elfaleh, N.; Kamoun, S. Structural characterization, vibrational studies and optical properties of a new luminescent organic-inorganic material $[C_6H_{20}N_3]BiI_6{\cdot}H_2O$. *J. Organomet. Chem.* **2016**, *819*, 95−102.
(19) Moskwa, M.; Bator, G.; Rok, M.; Medycki, W.; Miniewicz, A.; Jakubas, R. Investigations of organic-inorganic hybrids based on homopiperidinium cation with haloantimonates(iii) and halobismuthates(iii). Crystal structures, reversible phase transitions, semiconducting and molecular dynamic properties. *Dalton Trans* **2018**, *47*, 13507−13522.
(20) Li, L.; Liu, X.; Li, Y.; Xu, Z.; Wu, Z.; Han, S.; Tao, K.; Hong, M.; Luo, J.; Sun, Z. Two-Dimensional Hybrid Perovskite-Type Ferroelectric for Highly Polarization-Sensitive Shortwave Photodetection. *J. Am. Chem. Soc.* **2019**, *141*, 2623−2629.
(21) Li, L.; Shang, X.; Wang, S.; Dong, N.; Ji, C.; Chen, X.; Zhao, S.; Wang, J.; Sun, Z.; Hong, M.; Luo, J. Bilayered Hybrid Perovskite Ferroelectric with Giant Two-Photon Absorption. *J. Am. Chem. Soc.* **2018**, *140*, 6806−6809.
(22) Sun, Z.; Zeb, A.; Liu, S.; Ji, C.; Khan, T.; Li, L.; Hong, M.; Luo, J. Exploring a Lead-free Semiconducting Hybrid Ferroelectric with a Zero-Dimensional Perovskite-like Structure. *Angew. Chem., Int. Ed.* **2016**, *55*, 11854−11858.
(23) Sheldrick, G. SHELXT- Integrated space-group and crystal-structure determination. *Acta Crystallogr., Sect. A: Found. Adv.* **2015**, *71*, 3−8.
(24) Sheldrick, G. Crystal structure refinement with SHELXL. *Acta Crystallogr., Sect. C: Struct. Chem.* **2015**, *71*, 3−8.
(25) Dolomanov, O. V.; Bourhis, L. J.; Gildea, R. J.; Howard, J. A. K.; Puschmann, H. OLEX2: a complete structure solution, refinement and analysis program. *J. Appl. Crystallogr.* **2009**, *42*, 339−341.
(26) Atanasov, M.; Reinen, D. Density Functional Studies on the Lone Pair Effect of the Trivalent Group (V) Elements: I. Electronic Structure, Vibronic Coupling, and Chemical Criteria for the Occurrence of Lone Pair Distortions in ABX_3 Molecules (A = N to Bi; X = H, and F to I). *J. Phys. Chem. A* **2001**, *105*, 5450−5467.
(27) Atanasov, M.; Reinen, D. Predictive Concept for Lone-Pair Distortions- DFT and Vibronic Model Studies of $AX_n^{-(n-3)}$ Molecules and Complexes ($A = N^{III}$ to Bi^{III}; $X = F^{-I}$ to I^{-I}; n = 3−6). *J. Am. Chem. Soc.* **2002**, *124*, 6693−6705.
(28) Rademeyer, M. Bis(benzylammonium) hexachlorotin(IV). *Acta Crystallogr., Sect. C: Cryst. Struct. Commun.* **2004**, *60*, No. m55-m56.
(29) Shi, P. P.; Tang, Y. Y.; Li, P. F.; Liao, W. Q.; Wang, Z. X.; Ye, Q.; Xiong, R. G. Symmetry breaking in molecular ferroelectrics. *Chem. Soc. Rev.* **2016**, *45*, 3811−3827.
(30) Horiuchi, S.; Tokura, Y. Organic ferroelectrics. *Nat. Mater.* **2008**, *7*, 357−366.
(31) Tang, Y.-Y.; Zhang, W.-Y.; Li, P.-F.; Ye, H.-Y.; You, Y.-M.; Xiong, R.-G. Ultrafast Polarization Switching in a Biaxial Molecular Ferroelectric Thin Film: $[Hdabco]ClO_4$. *J. Am. Chem. Soc.* **2016**, *138*, 15784−15789.
(32) Jóźków, J.; Jakubas, R.; Bator, G.; Pietraszko, A. Ferroelectric properties of $(C_5H_5NH)_5Bi_2Br_{11}$. *J. Chem. Phys.* **2001**, *114*, 7239−7246.
(33) Piecha, A.; Białońska, A.; Jakubas, R. Structure and ferroelectric properties of $[C_3N_2H_5]_5[Bi_2Br_{11}]$. *J. Phys.: Condens. Matter* **2008**, *20*, 325224.
(34) Zhao, W. P.; Shi, C.; Stroppa, A.; Di Sante, D.; Cimpoesu, F.; Zhang, W. Lone-Pair-Electron-Driven Ionic Displacements in a Ferroelectric Metal-Organic Hybrid. *Inorg. Chem.* **2016**, *55*, 10337−10342.
(35) Piecha-Bisiorek, A.; Gagor, A.; Jakubas, R.; Cizman, A.; Janicki, R.Ł; Medycki, W. Ferroelectricity in bis(ethylammonium) pentachlorobismuthate(iii): synthesis, structure, polar and spectroscopic properties. *Inorg. Chem. Front.* **2017**, *4*, 1281−1286.
(36) Lee, D.; Lu, H.; Gu, Y.; Choi, S. Y.; Li, S. D.; Ryu, S.; Paudel, T. R.; Song, K.; Mikheev, E.; Lee, S.; Stemmer, S.; Tenne, D. A.; Oh, S. H.; Tsymbal, E. Y.; Wu, X.; Chen, L. Q.; Gruverman, A.; Eom, C. B. Emergence of room-temperature ferroelectricity at reduced dimensions. *Science* **2015**, *349*, 1314−1317.
(37) Balke, N.; Winchester, B.; Ren, W.; Chu, Y. H.; Morozovska, A. N.; Eliseev, E. A.; Huijben, M.; Vasudevan, R. K.; Maksymovych, P.; Britson, J.; Jesse, S.; Kornev, I.; Ramesh, R.; Bellaiche, L.; Chen, L. Q.; Kalinin, S. V. Enhanced electric conductivity at ferroelectric vortex cores in $BiFeO_3$. *Nat. Phys.* **2012**, *8*, 81−88.
(38) Xu, W. J.; Li, P. F.; Tang, Y. Y.; Zhang, W. X.; Xiong, R. G.; Chen, X. M. A Molecular Perovskite with Switchable Coordination Bonds for High-Temperature Multiaxial Ferroelectrics. *J. Am. Chem. Soc.* **2017**, *139*, 6369−6375.

DOI: 10.1021/acs.inorgchem.9b01793
Inorg. Chem. 2019, 58, 13953−13959